

# Surface model of the human red blood cell simulating changes in membrane curvature under strain

Philip W. Kuchel (✉ [philip.kuchel@sydney.edu.au](mailto:philip.kuchel@sydney.edu.au))

University of Sydney New South Wales

Charles D. Cox

Victor Chang Cardiac Research Institute

Daniel Daners

University of Sydney New South Wales

Dmitry Shishmarev

Australian National University

Petrik Galvosas

Victoria University Wellington

---

## Research Article

**Keywords:** Erythrocyte, 3-dimensional differential geometry, Mathematica, mechanosensitive Ca<sup>2+</sup> flux; Piezo1, surface triangularization

**Posted Date:** April 30th, 2021

**DOI:** <https://doi.org/10.21203/rs.3.rs-467222/v1>

**License:**  This work is licensed under a Creative Commons Attribution 4.0 International License.

[Read Full License](#)

---

# Surface model of the human red blood cell simulating changes in membrane curvature under strain

Philip W. Kuchel<sup>a\*</sup>, Charles D. Cox<sup>b,c</sup>, Daniel Daners<sup>d</sup>, Dmitry Shishmarev<sup>e</sup>, and Petrik Galvosas<sup>f</sup>

<sup>a</sup>*School of Life and Environmental Sciences, University of Sydney, Sydney, NSW, Australia.*

<sup>b</sup>*Victor Chang Cardiac Research Institute, Darlinghurst, Sydney, NSW, Australia.*

<sup>c</sup>*St Vincent's Clinical School, Faculty of Medicine, University of New South Wales, Sydney, New South Wales, Australia.*

<sup>d</sup>*School of Mathematics and Statistics, University of Sydney, Sydney, NSW, Australia.*

<sup>e</sup>*John Curtin School of Medical Research, Australian National University, Canberra, ACT, Australia.*

<sup>f</sup>*MacDiarmid Institute for Advanced Materials and Nanotechnology, School of Chemical and Physical Sciences, Victoria University Wellington, Wellington, New Zealand.*

**Running heading:** Mechanically distorted erythrocytes

**Correspondence:** Philip W. Kuchel

School of Life and Environmental Sciences

Building G08

University of Sydney

New South Wales, 2006

Australia

Email: [philip.kuchel@sydney.edu.au](mailto:philip.kuchel@sydney.edu.au)

Fax: (02) 9351 4726

**Keywords:** Erythrocyte; 3-dimensional differential geometry; *Mathematica*; mechanosensitive  $\text{Ca}^{2+}$  flux; Piezo1; surface triangularization

**Abbreviations:** 3D, 3-dimensional; NMR, nuclear magnetic resonance; RBC, red blood cell

## Abstract

The highly deformable red blood cell (erythrocyte; RBC) responds to mechanically imposed shape changes with enhanced glycolytic flux and cation transport. Such morphological changes are produced experimentally by suspending the cells in a gelatin gel, which is then elongated or compressed in a special apparatus inside an NMR spectrometer. However, direct mathematical predictions of the shapes of the morphed cells have not been reported before. We used recently available functions in *Mathematica* to triangularize and then compute four types of curvature. The RBCs were described by a previously presented quartic equation in three dimensional (3D) Cartesian space. A key finding was the extent to which the maximum and minimum Principal Curvatures were localized symmetrically in patches at the poles or equators and distributed in rings around the main axis of the strained RBC. The simulations, on the nano-metre to micro-meter scale of curvature, suggest activation of only a subset of the intrinsic mechanosensitive cation channels, Piezo1, during experiments carried out with controlled distortions that persist for many hours. This view is consistent with a recent proposal for non-uniform distribution of Piezo1 molecules around the RBC membrane. On the other hand, if the curvature that gates Piezo1 is at a much finer length scale, then membrane tension will determine local curvature and micron scale curvature as described here will be less likely to influence Piezo1 activity.

The geometrical reorganization of the simulated cytoskeleton helps understanding of the concerted metabolic and cation-flux responses of the RBC to mechanically imposed shape changes.

## Introduction

Our aim is to convey a sense of scale of the distribution of proteins in the membrane and adjacent cytoskeleton, relative to the whole human red blood cell (RBC); and to graphically represent changes in membrane curvature on the ~1 nm to ~10  $\mu\text{m}$  scale, brought about by the systematic straining of these cells. This study was motivated by the quest for the geometrical and mechanistic basis of recent findings on mechanically distorted RBCs, made by using nuclear magnetic resonance (NMR) spectroscopy with stretched and compressed gels [1, 2]. The rates of glycolysis and transmembrane exchange of cations in RBCs are enhanced when these cells, suspended in gelatin gel, are stretched or compressed. The effects occur only when the medium contains  $\text{Ca}^{2+}$  ions; and the cells' responses are attributed to the activation of the mechanosensitive cation channel, Piezo1, when the plasma membrane is distorted [3-7]. The NMR-based cation-flux estimates are in the same range as measurements made by electrophysiological means, performed on whole RBCs and membrane patches (patch clamping) (e.g., [6]). However, because the electrophysiological measurements typically occur over seconds (of a transient response to shape change), while the NMR experiments can last for hours a different property of channel opening and closure is in operation [1, 2, 8]; the latter is referred to a 'channel fatigue' e.g., [9].

The Piezo1 three-arm (triskelion) structure spans a relatively large ~23 nm diameter membrane patch; this has been measured from images obtained with cryo-electron microscopy [10-12]. Such imaging provides an indication of the likely values of curvature that are required to activate the channel. The current model suggests that the channel is curved in the resting state and flattens as membrane tension increases, which opens the channel [13]. Therefore, when inspecting the alteration of the average extent of membrane curvature, when an RBC is distorted, we might expect an increase in the fraction of the total membrane area that has lower curvature; since such altered topology (induced flatness) appears to cause activation of Piezo1. To quantify the alteration of membrane curvature that is brought about by stretching an idealized RBC, we employed a geometrical *strain field*, in which an RBC is elongated by a specified extent, denoted by  $\xi$ . In addition, we considered the variation of the angle of rotation of RBCs relative to the direction of the imposed strain field, prior to "switching the strain field on" (imposing stretch). This is relevant to describing the state-of-affairs of RBCs suspended in liquid gelatin prior to gelation, because the cells are known to have random orientations, which persist while in the gel state [14]. The mathematical model used in these analyses captures the

key micro-anatomical dimensions of the discocyte that typify a human RBC (and in most other mammals other than the camelidae) [15].

Mathematical definitions of curvature of three dimensional (3D) surfaces are a major concern of differential geometry [16, 17]; it is obvious that complicated formulae have become more accessible since the advent of symbolic computation, most notably in software packages like *Mathematica* [18, 19]. Euler rotation matrices and strain tensors were applied to bring about the simulated RBC distortions (morphing), taking care to invoke the relevant inverse functions in the definition of the transformed shape function, and the curvature functions; again, *Mathematica* generated algebraic expressions symbolically. This remarkable outcome, despite the highly complicated forms, meant that the expressions were readily evaluated to give estimates of curvatures. The ability to triangularize\* the mathematically specified surface of the RBC (in *Mathematica*) meant that the relative size of the cytoskeletal triangular (also referred to as hexagonal) mesh was able to be visualized in practicable computation times (minutes) [18]. (\*Aside: we use the term *triangularization* as opposed to triangulation to distinguish the operation from the trigonometric procedure used in surveying, and cartography etc.)

## Theory of Methods

**RBC shape.** There have been several expressions presented for the shape of the RBC including one based on the minimization of the bending energy of a dual layer membrane [20]. The mathematical expression for the RBC discocyte used here is close to those in [20], and it is a continuous degree-4 surface that can be written either in Cartesian or disc-cyclide coordinates, making it versatile for numerical exploration [15]. The shape is constrained by three principal distances, the main diameter,  $d$ , the thickness at the centre of the dimples,  $b$ , and the maximum thickness (height) near the periphery of the cell,  $h$  (see Figure 1 for the first of many examples here):

$$(x^2 + y^2 + z^2)^2 + P(x^2 + y^2) + Qz^2 + R = 0 \quad , \quad (1)$$

where,

$$P = -\frac{d^2}{2} + \frac{h^2}{2} \left( \frac{d^2}{b^2} - 1 \right) - \frac{h^2}{2} \left( \frac{d^2}{b^2} - 1 \right) \left( 1 - \frac{b^2}{h^2} \right)^{\frac{1}{2}} \quad , \quad (2)$$

$$Q = P \frac{d^2}{b^2} + \frac{b^2}{4} \left( \frac{d^4}{b^4} - 1 \right) \quad , \quad (3)$$

$$R = -P \frac{d^2}{4} - \frac{d^4}{16} . \quad (4)$$

The mean volume of a normal human RBC is 86 fL, while the surface area is variously stated to be  $137 \pm 17$  or  $143 \mu\text{m}^2$  [21, 22]. Thus, when  $d = 8 \mu\text{m}$ ,  $b = 1 \mu\text{m}$ , and  $h = 2.12 \mu\text{m}$ , the model gives a volume of 86 fL and a surface area of  $128 \mu\text{m}^2$ . We gave precedence to the correct volume over the predicted smaller surface area in the above range of  $120 - 154 \mu\text{m}^2$ .

**Triangularization of the surface.** While Eq. 1 is readily graphed in *Mathematica*, a representation of the cell's cytoskeleton requires partitioning the surface with a known number of struts (edges) in the geodetic-dome-like closed polyhedron. In a human RBC, the struts of the mesh consist of head-to-head associated two hetero-dimers of  $\alpha$ - and  $\beta$ -spectrin, with junctional complexes of 12-14 actin monomers bound as a short, twisted filament. There are  $\sim 121,000$  edges [23] so in *Mathematica* the Option, MaxCellMeasure in the BoundaryDiscretizeRegion function could be manually adjusted to make the number of edges in the polyhedron very close to this value (see the Supplementary Information for a Notebook implementation).

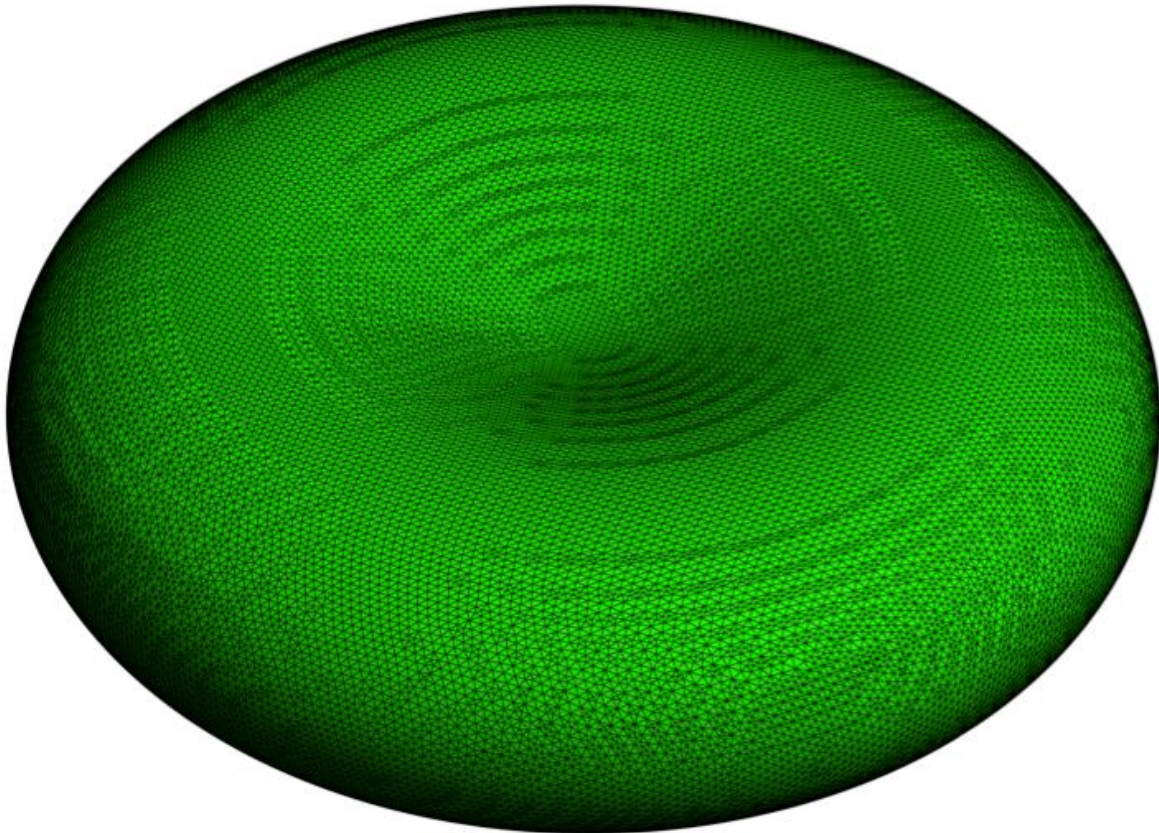


**Figure 1.** Triangular mesh of the RBC drawn to scale in its biconcave-disc, using Eq. 1 in *Mathematica*. The triangulation was with `BoundaryDiscretizationRegion`, applied to `ImplicitRegion` (Supplementary Information). Number of edges = 120,042 and `MeshCoordinates` gave 40,136 points and 80,268 triangles. Green colouring was chosen over red (the natural choice for an RBC) for ease of visualizing the mesh. Notebook 2 has the *Mathematica* script used to generate this graphic.

**Shape transformation.** We emulated the distortion of RBCs suspended in stretched gelatin gel by specifying that a geometrical strain field was applied in one direction, chosen to be along the  $z$ -axis. This equates to what applies in real NMR experiments [1, 2]. It is not possible, experimentally, to align all the RBCs in gelatin media prior to or after gelation, so the members of the population of RBCs assume all possible orientations of their axes of symmetry in the strain field. Therefore, we considered three orientations as *representative* of all those that are possible (see Discussion for additional comment).

*Euler rotation matrix:* To alter RBC orientation, the independent variables in Eq. 1 were transformed, by rotation about the  $x$ -axis by an angle  $\theta$ , using an Euler rotation matrix [24]:

$$R_\theta = \begin{pmatrix} 1 & 0 & 0 \\ 0 & \cos\theta & -\sin\theta \\ 0 & \sin\theta & \cos\theta \end{pmatrix}, \quad (5)$$

where  $\theta = 0$  specifies the original position/orientation.

*Strain tensor:* This mathematical object is a matrix that invokes volume preserving elongation of a Cartesian body in the direction of the  $z$ -axis:

$$S_\xi = \begin{pmatrix} \frac{1}{\sqrt{\xi}} & 0 & 0 \\ 0 & \frac{1}{\sqrt{\xi}} & 0 \\ 0 & 0 & \xi \end{pmatrix}, \quad (6)$$

where  $\xi = 1$  specifies the original shape.

*Inverse affine transformation of Eq. 1:* The requisite overall coordinate-transformation matrix was derived symbolically in *Mathematica* with the following function (note the standard matrix product denoted by  $\cdot$ ).

```
trf = InverseFunction[AffineTransform[S\xi . Rθ]]
```

followed by 'threading' the transformation through the discocyte expression (see the Supplementary Information for further explanation of the symbols and the complete *Mathematica* Notebook):

```
(x² + y² + z²)² + pP (x² + y²) + qQ z² + rR /. Thread[{x, y, z} → trf[{x, y, z}]] // Simplify  
.
```

(7)

and this yielded the shape-transformed Eq. 1:

$$\begin{aligned}
& \frac{(z^2 + (x^2 + y^2) \xi^3)^2}{\xi^4} \\
& - \frac{\left( b^6 + 2 d^4 \left( -1 + \sqrt{1 - \frac{b^2}{h^2}} \right) h^2 + b^2 \left( d^4 - 2 d^2 \left( -1 + \sqrt{1 - \frac{b^2}{h^2}} \right) h^2 \right) \right) (z \cos[\theta] - y \xi^{3/2} \sin[\theta])^2}{4 b^4 \xi^2} \\
& - \frac{\left( b^2 d^2 + (b^2 - d^2) h^2 - (b^2 - d^2) \sqrt{1 - \frac{b^2}{h^2}} h^2 \right) (x^2 \xi^3 + (y \xi^{3/2} \cos[\theta] + z \sin[\theta])^2)}{2 b^2 \xi^2} \\
& - \frac{d^4}{16} + \frac{d^2 \left( b^2 d^2 + (b^2 - d^2) h^2 - (b^2 - d^2) \sqrt{1 - \frac{b^2}{h^2}} h^2 \right)}{8 b^2} = 0
\end{aligned} \tag{8}$$

Then, the triangularization of the surface was performed as follows:

```

rbc0 = ImplicitRegion[(x^2 + y^2 + z^2)^2 + pP (x^2 + y^2) + qQ z^2 + rR < 0];
Thread[{x, y, z} \[Rule] trf[{x, y, z}]], {{x, -7, 7}, {y, -7, 7}, {z, -7, 7}}];
bmr0 = BoundaryDiscretizeRegion[rbc0, MaxCellMeasure \[Rule] 0.00858, AspectRatio \[Rule] 1];
RBCVolume = RegionMeasure[bmr0];
RBCArea = RegionMeasure[RegionBoundary[bmr0]];
meshCoords = MeshCoordinates[bmr0];
meshTriangles = MeshPrimitives[bmr0, 2];
gphGreenPlus = Graphics3D[{RGBColor[0, 1, 0], Opacity[0.9],
  meshTriangles}, Boxed \[Rule] False]

```

.

.

The function `RegionMeasure` applied to the boundary-discretized region gave the RBC volume; and the functions `RegionMeasure[RegionBoundary[bmr0]]` yielded the area of the RBC. The coordinates of the nodes of the mesh, and the list of all triangles, were obtained with the functions `MeshCoordinates` and `MeshPrimitives`. Finally, `MeshTriangles` was plotted by using `Graphics3D` (Figure 1).

**Curvature.** Representing shape and curvature are primary objectives of differential geometry [16], and modern computation with *Mathematica* provides a way of generating curvature expressions for surfaces that are defined implicitly by equations like Eq. 1. And, even more remarkably, those transformed to complicated expressions like Eqs. 8 and 9.

A non-planar surface in three dimensions has a tangent plane and a normal vector at a specified point. In general, the curvature of the surface differs in one direction, versus one at right angles to it. The shapes of these surfaces can be illustrated with the particular example of the

hyperbolic paraboloid (saddle) [16]. Such a graphical rendering is shown in Supplementary Information, Figure S1. The observation of, in general, two Principal Curvatures motivates the implementation of expressions that describe the curvature of the surface at a given point on the RBC. The fact that there are several ways of describing curvature of a surface may not be immediately obvious ; but in general there are four expressions that have been explored in the theory of 3D differential geometry [16].

**Curvature expressions.** We begin the presentation of the operations that are required to calculate the types of curvatures of the RBC surface by defining  $F[x,y,z]$  from Eq. 1:

$$F[x,y,z] \equiv (x^2 + y^2 + z^2)^2 + P(x^2 + y^2) + Qz^2 + R = 0 \quad . \quad (10)$$

Four operations are to be carried out on  $F[x,y,z]$  to make up the requisite expressions: (1) The gradient of  $F$ ,  $\nabla F[x,y,z]$ , is a vector of partial derivatives of  $F$  with respect to each of the independent Cartesian variables:

$$\nabla F[x,y,z] = (F_x, F_y, F_z) \quad . \quad (12)$$

(2) The Hessian of  $F$ ,  $H[F]$ , is a  $3 \times 3$  matrix of second order partial derivatives of  $F$ :

$$H[F] = \begin{pmatrix} F_{xx} & F_{xy} & F_{xz} \\ F_{yx} & F_{yy} & F_{yz} \\ F_{zx} & F_{zy} & F_{zz} \end{pmatrix} \quad . \quad (13)$$

(3) The cofactor or adjugate matrix, denoted by  $H^*[F]$  is defined as:

$$H^*[F] = \begin{pmatrix} \text{Cofactor}(F_{xx}) & \text{Cofactor}(F_{xy}) & \text{Cofactor}(F_{xz}) \\ \text{Cofactor}(F_{yx}) & \text{Cofactor}(F_{yy}) & \text{Cofactor}(F_{yz}) \\ \text{Cofactor}(F_{zx}) & \text{Cofactor}(F_{zy}) & \text{Cofactor}(F_{zz}) \end{pmatrix} \quad , \quad (14)$$

where  $\text{Cofactor}(F_{xx})$  for each of the second derivatives in Eq. 13 is a matrix of determinants [25].

(4) Finally, the trace of the Hessian matrix is required; this is simply the sum of the three terms in the leading diagonal of  $H[F]$  (Eq. 13); it is the Laplace operator of  $F$ .

*Gaussian curvature  $K_G$ :* The Gaussian Curvature is expressed in terms of the vector of partial derivatives, its transpose, and the cofactor matrix of the Hessian [16, 17]:

$$K_G = \frac{\nabla F \cdot H^*[F] \cdot \nabla F^T}{|\nabla F|^4} \quad . \quad (15)$$

*Mean curvature  $K_M$ :* This is given by,

$$K_M = \frac{\nabla F \cdot H[F] \cdot \nabla F^T - |\nabla F|^2 \text{Trace}[H]}{2 |\nabla F|^3} . \quad (16)$$

*Principal curvatures  $k_1$  and  $k_2$ :* They are the smallest and largest curvatures at a given point. It appears obtuse to define the Principal Curvatures after the other two, but it is computationally more efficient to do so [16, 17]:

$$k_1 = K_M + \sqrt{K_M^2 - K_G^2} , \quad (17)$$

$$k_2 = K_M - \sqrt{K_M^2 - K_G^2} . \quad (18)$$

The relationships are  $K_G = k_1 k_2$ , and  $K_M = \frac{k_1 + k_2}{2}$ , the latter explaining the term Mean Curvature.

### Implementation of Eqs 15-18 for the RBC.

*Average at the three vertices:* The next step after triangularization (as shown in Figure 1) was to assign the values of curvature to each triangular face. This was done by applying Eqs. 15-18 to the vertices of each of the triangles and then averaging the three values.

*Average at the centroid:* An alternative treatment was to determine the positions of the centroid (centre of gravity) of each triangle and apply Eqs 15-18 to those:

$$\text{Centroid}[x,y,z] = (\text{vertex1}[x,y,z] + \text{vertex2}[x,y,z] + \text{vertex3}[x,y,z]) / 3 . \quad (19)$$

*Weighted average curvatures:* Because the area of the triangles in any triangularization vary, as seen in the histogram of Figure 2, the average of the curvatures of a set of triangles must be the weighted average. The weighting factor is the area of the triangle relative to the total area of all the triangles in the set:

$$\text{wtAverageCurvature} = \frac{\sum_{i=1}^N \text{area}_i \text{curvature}_i}{\sum_{i=1}^N \text{area}_i} , \quad (20)$$

where the area of each triangle is given by the ‘cross product formula’ from vector analysis [26]. The differences between the position vectors of each vertex,  $v_1, v_2, v_3$  are the side vectors of the triangle,  $\times$  denotes the vector cross product, and  $\| \cdot \|$  denotes the norm:

$$\text{area} = (1/2) |(v_2 - v_1) \times (v_3 - v_1)| . \quad (21)$$

## Results

### Triangularization.

*Euler test:* The triangularization shown in Figure 1 was closed (no gaps), with the number of edges E, faces (F; triangles) and vertices (V; mesh points) conforming to Euler's formula  $F - E + V = 2$  [27]; the 2 is a topological invariant called the ‘Euler characteristic’ and is typically denoted by  $\chi$ .

*Gauss-Bonnet theorem test:* The Total Curvature which is the integral of the values of the Gaussian Curvature,  $K_G$ , over a closed surface (like that used to describe the RBC), evaluates to  $4\pi$ ; specifically it is  $2\pi \chi$  [16]. This was indeed closely approximated by summing the product of  $K_G$  (the mean of the three values of each triangle) and its area, across all triangles in the mesh. An example of the analysis is given in Notebook 5, Supplementary Information.

*Triangles per mesh point:* Detailed inspection of the mesh showed that in the vast majority of cases a single mesh point was met by six triangles; but there were a few instances of five and seven triangles sharing one vertex. These points appeared to be randomly dispersed on the surface. If the instances of such sharp triangles were high this could cause problems with the finite element approximation of the surface area; but there was not a problem as noted above in relation to the Gauss-Bonnet Theorem test. On the other hand such aberrant triangles are not a "good" representation of the spectrin mesh according to recent microscopic image analysis [23, 28].

*Orientation:* It was important to test the fidelity to the triangularization algorithm in generating the same RBC volume and area, and curvature estimates when the RBC was rotated about the  $x$ -axis (and, by symmetry, any other rotations about lines through the origin in the  $x,y$ -plane) in the Cartesian coordinate system using Eq. 5. Specifically, the distribution of edge-lengths should not change when  $\theta$  is varied, and this was reliably achieved.

*Edge length:* The next step was to compute the distribution of edge lengths, in order to study how these edges, which could be thought of as modelling the spectrin network, might imply that the spectrin is either stretched or compressed. Figure 2 shows the distribution of sides in Figure 1, first at a resolution of 20 linearly space bins. The distribution is slightly skewed to the left, but it is unimodal; however, the inset which was based on 200 bins now appears to be at least trimodal (see Discussion).

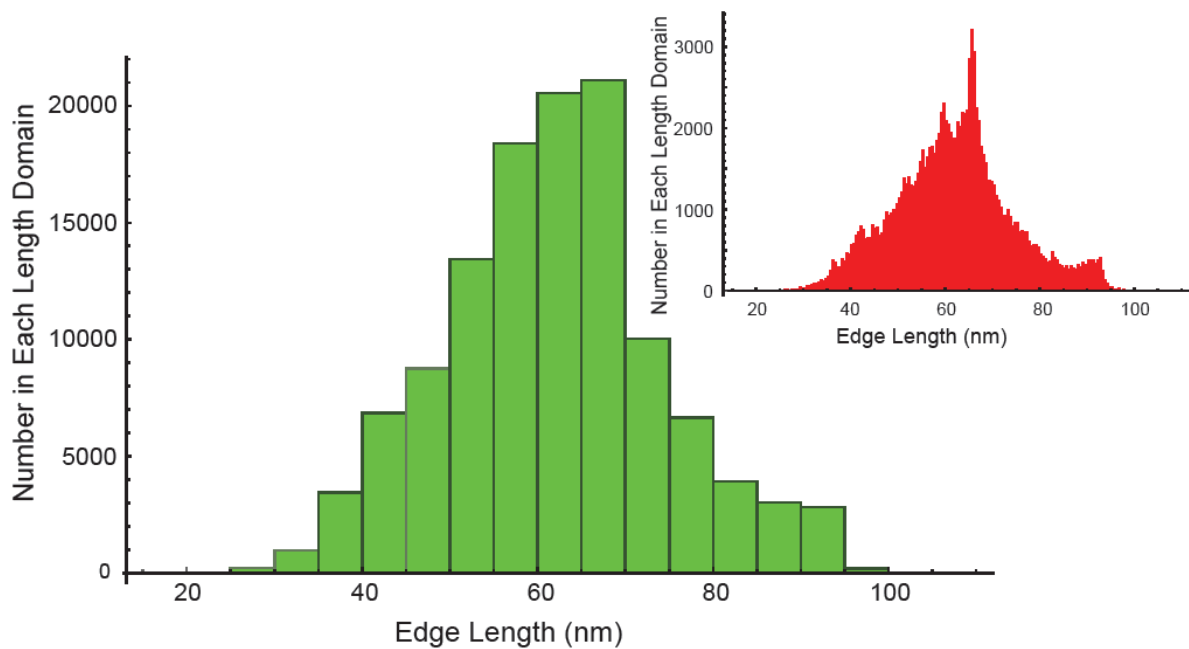


**Figure 2.** Data from the mesh in Fig.1 showing the length-distribution histogram of edges in 20 bins (green); and, 200 bins (red inset). The mean edge length overall was 62 nm. The median bin (tallest green pillar) contained 38% of the total bin contents and spanned 60 - 65 nm; while the two most abundant bins spanning 60 - 70 nm contained 75% of the edge lengths. Notebook 2 has the *Mathematica* script used to generate this graphic.

*Triangle area distribution:* Another feature of the surface triangularization, that is of biophysical importance, is the area of each triangle and whether this is consistent with the known span of membrane proteins that are corralled in the network. Figure S2a shows the separate triangularization of the RBC which (as for Figure 1) clearly indicates a range of shapes and sizes of the triangles. Sorting the triangles according to area showed a span from 0.0094 to 3431 nm<sup>2</sup>. When subdivided linearly into 10 bins it was seen that the 6<sup>th</sup> bin contained the most triangles (27,541) with a mean area of 1873 nm<sup>2</sup>; in other words 40.3% of the total area of 128

$\mu\text{m}^2$  had this mean area, while the mean area of a triangle across the whole cell was  $1575 \text{ nm}^2$ . The size distribution is shown graphically in Figure S3.

**Curvature mapping.** A primary aim was to devise a means of displaying (mapping) the distribution of curvature(s) on the surface of the RBC. For this, a colour-coding program was written. Each triangle from the triangulation was stored in one of 10 value-domains, according to whichever of the attributes was to be mapped. Figure 3 shows an undistorted RBC with its axis of symmetry normal to the  $x,y$ -plane, and for which the average of the curvatures at each of the three vertices of each triangle was assigned.

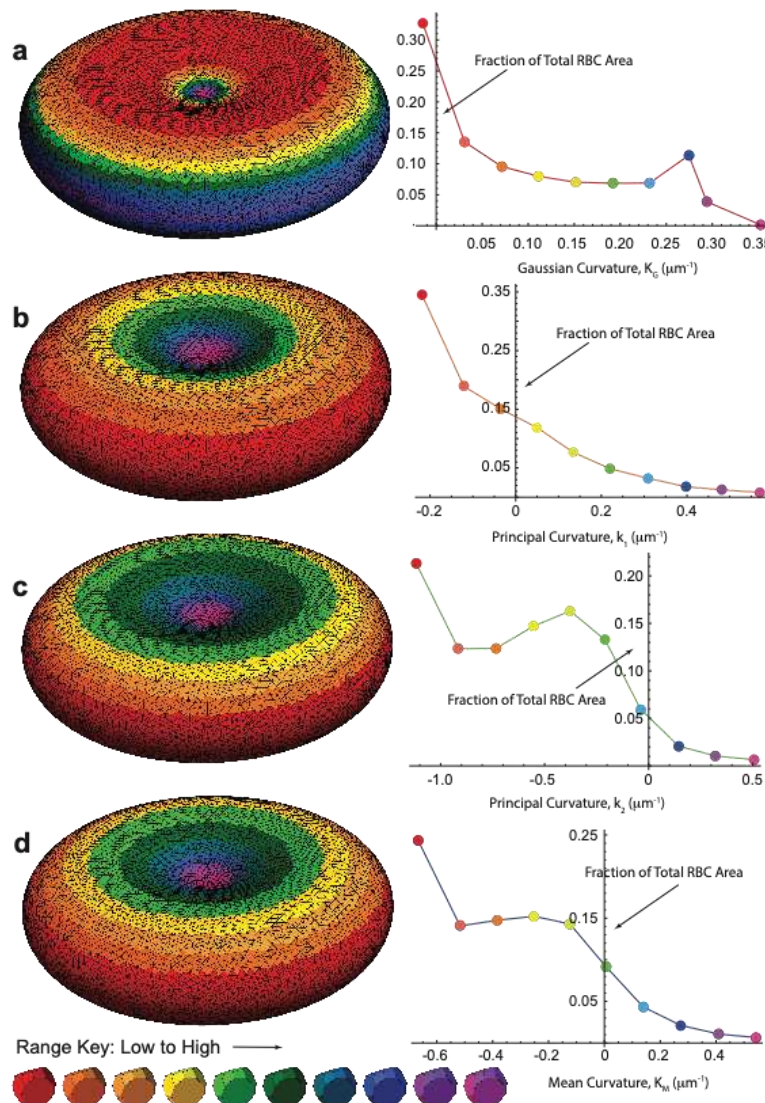


**Figure 3.** Positional dependence of the four types of curvature on the surface of the model-RBC. **(a)** Gaussian Curvature; **(b)** Principal Curvature (maximum),  $k_1$ ; **(c)** Principal Curvature (minimum),  $k_2$ ; and **(d)** Mean

Curvature. On the right of each cell is the graph of mean value (of the respective curvature) versus the fraction of the RBC area that has the curvature in a specified sub-domain of values. Specifically, the minimum and maximum values of each curvature were identified, then the whole domain of values was divided linearly into 10 sub-domains (bins) with each assigned a colour-code as shown in the given Range Key. The area of each triangle was computed (Theory of Methods; and Notebook 2) so the total area occupied by triangles in a given bin was able to be expressed as a fraction of the total RBC area,  $128 \mu\text{m}^2$ . For speed of computation the triangularization was made with fewer mesh points than for Figure 1, specifically 13640 triangles and 6822 mesh points.

**Rotation and Strain.** The affine transformation, which combines both rotation and strain, produced shape changes as those shown in Figure 4. For this figure the RBC was rotated by  $45^\circ$  from the  $x,y$ -plane and then increasingly stretched.

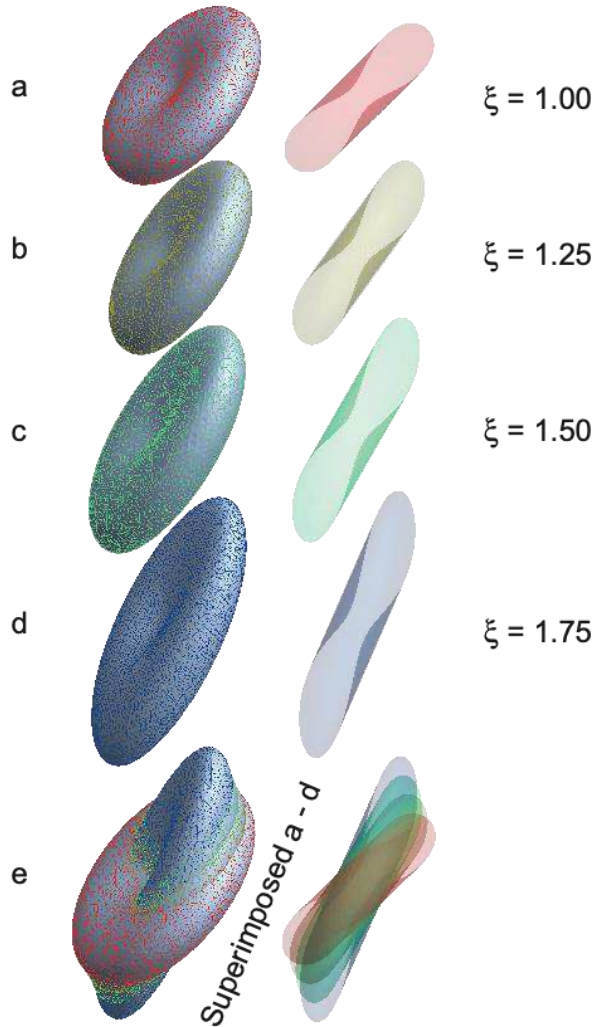


**Figure 4.** RBC rotated through  $45^\circ$  about the  $x$ -axis, relative to a linear strain field imposed in the  $z$ -direction. (a) No elongation,  $\xi = 1$ ; (b) stretched by 25%,  $\xi = 1.25$ ; (c) stretched by 50%,  $\xi = 1.50$ ; (d) stretched by 75%,  $\xi = 1.75$ ; and (e) showing the relative elongation and concomitant narrowing of the RBCs by superimposing the

images. Colour coding was used to provide distinction between the RBCs in e. In the boundary discretization MaxCellMeasure was set to 0.1 giving ~8,000 mesh points.

On stretching (in the z-direction) the RBC was elongated and became narrower, an effect best seen in the overlapping images in Figure 4e. However, the width of the RBC at the dimples and the maximum curvature at the rim both increased, as if the opposite faces of the cell were being pulled apart.

**Volume and surface area during distortion.** The surface area of an RBC declines with age in the blood circulation [29, 30].

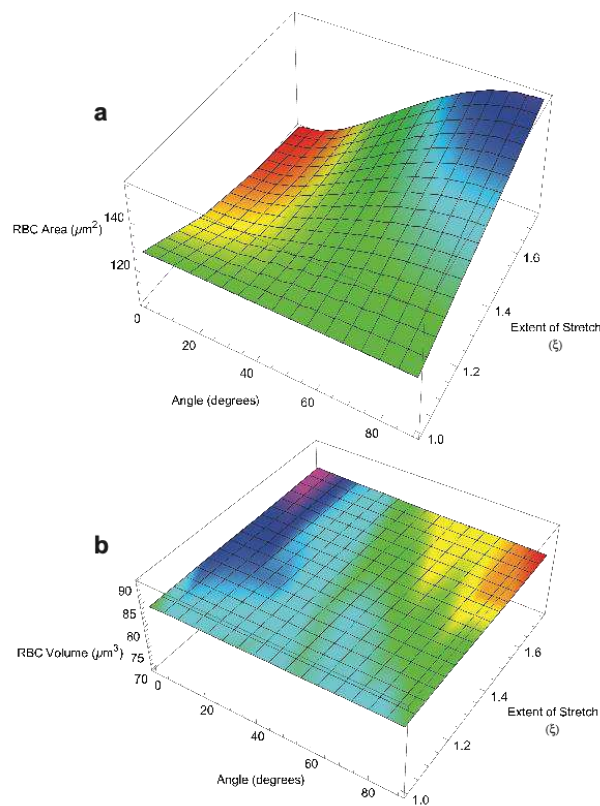


**Figure 5.** Dependence of RBC surface area (a) and volume (b) on rotation about to the  $x$ -axis ( $\theta$ ) and stretching along the  $z$ -axis ( $\xi$ ).

It is also known that an RBC's surface area cannot be increased by more than ~15% before it ruptures; this was discovered in studies with RBCs swelling in hypotonic media [31]. In our own experiments with RBCs suspended in gelatin gel that is then stretched, haemolysis is very extensive with two-fold stretching ( $\xi = 2$ ) (unpublished results). Therefore, it was important to

explore the volume and surface area inter-relationships that are brought about by the affine transformation (Eqs. 5 and 6).

Figure 5a shows that the surface area decreases on stretching if the RBC lies across the strain field; but it increases by up to 21% as the cell is stretched by 75% ( $\xi = 1.75$ ) when aligned with its disc-plane parallel to the strain field. Meanwhile, the volume of the RBC scarcely changed under all the angles or orientation and extents of stretching explored here (Figure 5b).

Overall, we concluded from Figure 5 that RBCs sustain increased *or* decreased surface area depending on their initial orientation in the gel on stretching the sample, while the volume did not change significantly. The extent of area change is much less than would occur with a sphere; and this helps explain why the biconcave disc shape has been naturally selected. Specifically, the particular shape enables volume and surface area preservation during passage of the RBC through the capillaries of the peripheral tissues and lungs [2, 29, 30, 32].

**Colour-coded curvatures for different values of  $\theta$  and  $\xi$ .** Figure 6 shows RBCs that were tilted at 45° around the  $x$ -axis and progressively strained from no extension to a maximum of  $\xi = 1.75$ . The changes in curvature are indicated by the changes in colour; the most notable feature for the Gaussian curvature ( $K_G$ ) is the increasing dominance of areas of red denoting increased area of lower values as the RBCs are stretched. On the other hand, the intermediate values (green) dominate the area of the values of  $k_1$  (the maximum Principal Curvature). Numerous other comparisons can be made, as are taken up in the Discussion.

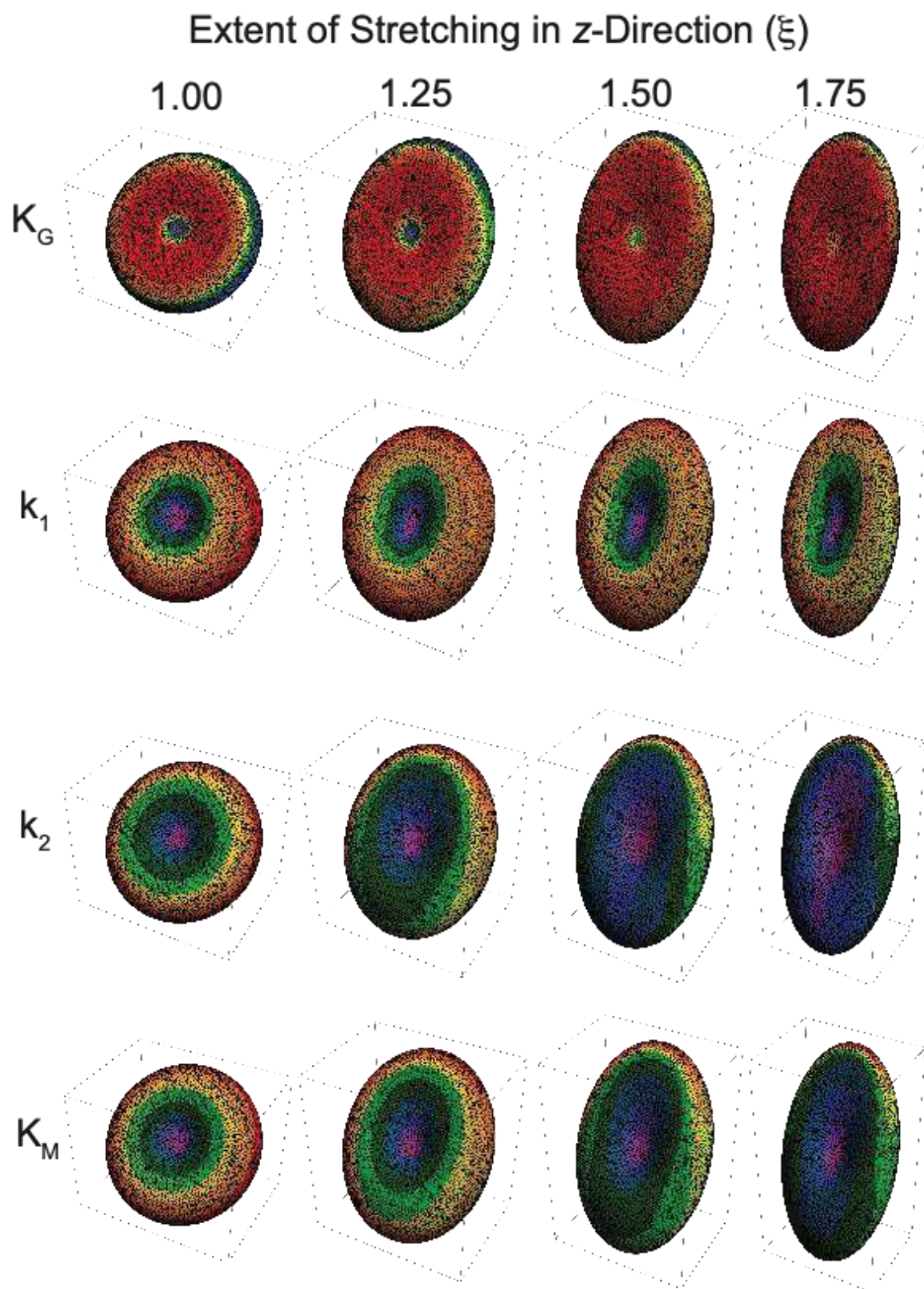


**Figure 6.** Curvatures of RBC rotated 45° around the  $x$ -axis and stretched in the  $z$ -direction by the extents ( $\xi$ ) indicated above.

Another way of depicting the changes in curvature with orientation and strain is via a form of histogram shown in Figure 7. The graphs show the fraction of the RBC area that is occupied by triangles with curvature (for each of the four types) in the neighbourhood of the mean values that correspond to 10 bins, arranged uniformly between the minimum and maximum values of the curvature.

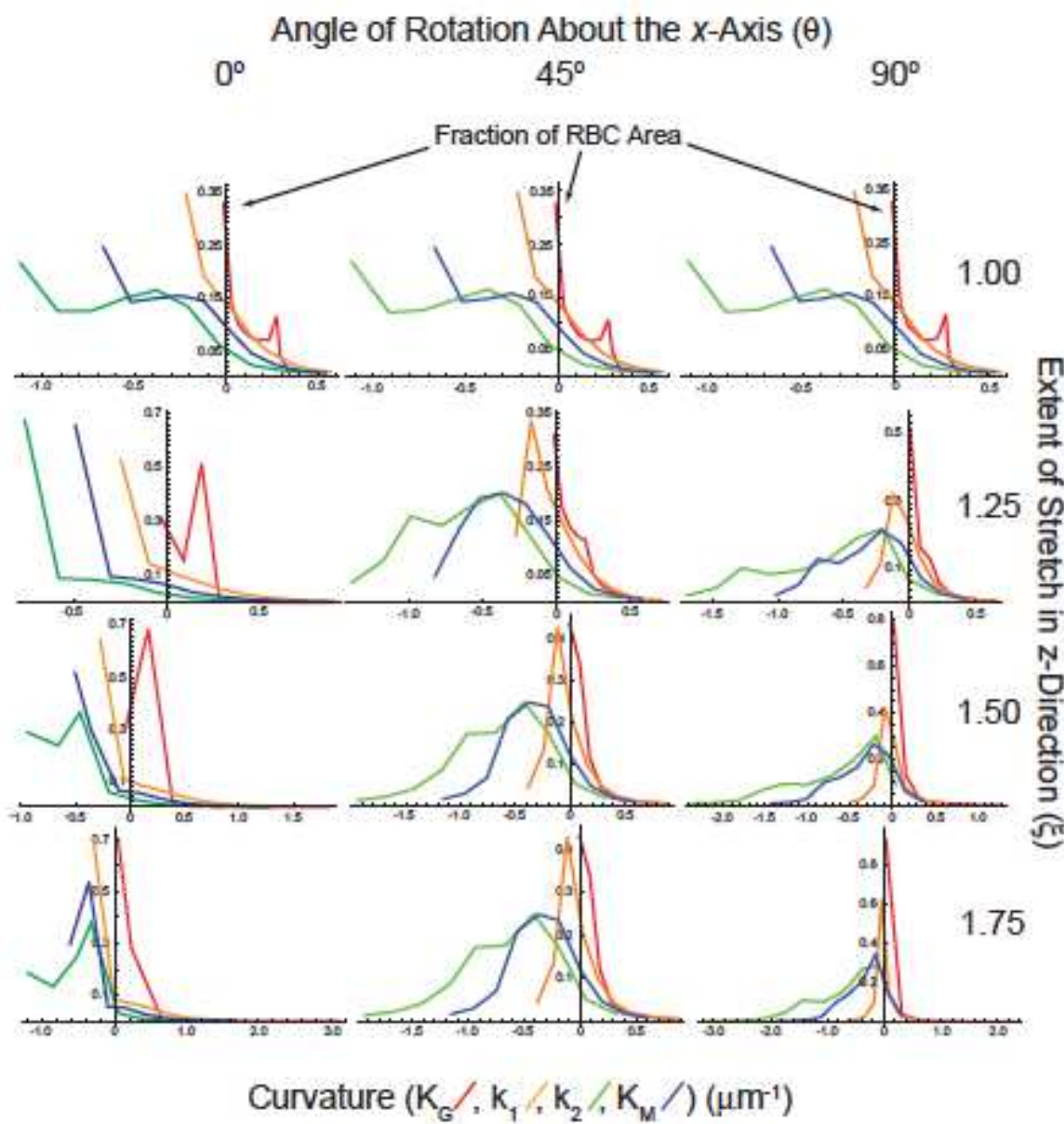


**Figure 7.** Curvature graphs of an RBC rotated at  $0^\circ$ ,  $45^\circ$  and  $90^\circ$  around the  $x$ -axis and stretched in the  $z$ -direction by the extents ( $\xi$ ) indicated on the right. The colours of the polygonal plots indicate: Gaussian Curvature  $K_G$ , red; Principal Curvature (maximum),  $k_1$ , orange; Principal Curvature (minimum),  $k_2$ , green; and Mean Curvature  $K_M$ ,

blue. Each discontinuity of the polygons denotes the mean value in curvature of the bin in the given curvature domain.

The values of the curvatures span different ranges in all scenarios of orientation and strain. When there is no strain (top row of Figure 7, and Figure 3) the triangles with  $k_1$  (orange line) of smallest value occupy the largest area. When the RBCs at  $0^\circ$  are stretched the minimum of  $k_1$  decreases in value but occupies a much larger area of the cell as stretching is increased. Another notable feature at  $45^\circ$  orientation is the shift in  $k_2$  and the mean curvature (green and blue lines) to larger values as stretching was increased, with the maximum area occupied by triangles of intermediate values. Also, there is a clearly defined maximum value in these polygonal graphs. For the RBCs at  $90^\circ$  orientation  $k_1$  and  $k_2$  both decrease with increased stretching with the maximum area occupied by large values. Overall, the patterns of all four polygonal graphs shift progressively as stretching is increased, but at each of the angles of orientation the patterns are distinctly different.

This is but a snapshot of three angles; for a continuous distribution of angles we would expect a smooth transition from the left hand column of polygonal graphs through the middle column to the right hand column.

**Edge length distribution as a function of extent of stretching.** Figure 8 shows that for  $0^\circ$  orientation the median value of edge length of the triangularization decreased on stretching by 75% more than the original value. This is consistent with the fact that Figure 5 shows that for  $\theta = 0^\circ$  the surface area decreased with increasing  $\xi$ . The main feature for the RBCs at  $45^\circ$  is the emergence of a broad bimodal distribution of edge lengths that is most clearly evident in the bottom of the middle column of the histograms. On the other hand, when the RBCs were at  $90^\circ$  the distribution of edge lengths remained relatively narrow all the way to  $\xi = 1.75$ . From Figure 5 it is at this orientation that most increase in area took place and it is especially clear in the bottom right-hand histogram that the median edge length was  $\sim 70$  nm; this is similar to the second maximum in the second column. Consistent with this observation is that both RBC orientations display increases in surface area as well (Figure 5).

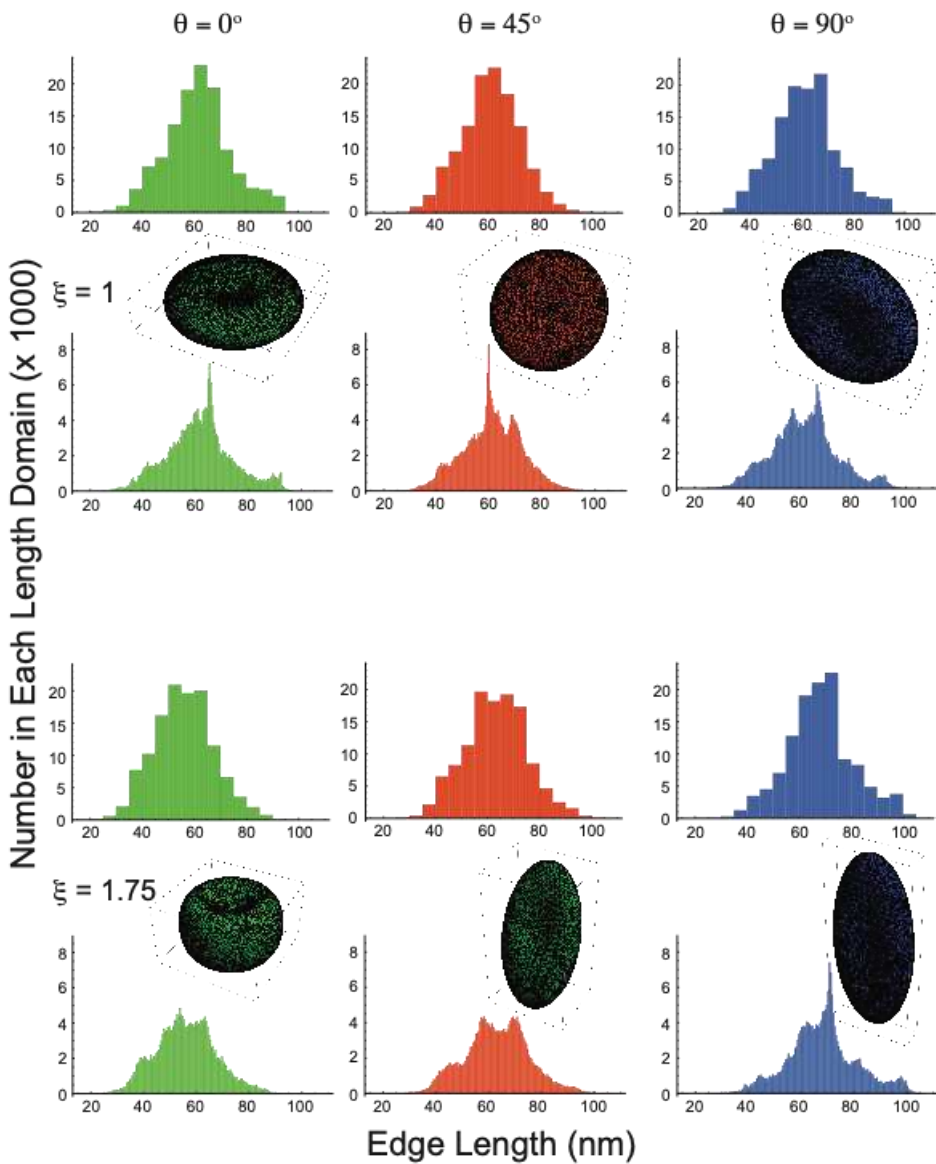


**Figure 8.** Histograms of the lengths of the 121,000 edges in the triangularization of an RBC at each of three rotations about the  $x$ -axis with no stretching ( $\xi = 1$ ), and 75% stretching ( $\xi = 1.75$ ). The colour coding was used to distinguish the three groups of data according to the rotations: green  $0^\circ$ , red  $45^\circ$ , and blue  $90^\circ$ . The bin numbers were 20 and 200 for the upper and lower pair of histograms at each value of stretching,  $\xi$ , respectively. The insets show the RBC shapes from which the histograms were made; they are the same as given in Figures 4, S4 and S5.

## Discussion

**Triangularization.** The fully extended  $\alpha$ - and  $\beta$ -spectrin heterotetramer has an end-to-end length of  $\sim 200$  nm [23]; but the filaments of unstretched RBC membranes have an average distance between the nodal F-actin helices of  $60 - 70$  nm [33], and up to  $85$  nm [28]. The

automatic triangulation, that we used here to model the RBC cytoskeleton was controlled to correspond to the 121,000  $\alpha$ - and  $\beta$ -spectrin heterotetramers; and this gave  $\sim$ 65 nm as the mean value of the distance between two neighbouring nodes. This would imply that native spectrin has its filaments in a bent or serpentine form that more than halves the end-to-end distance of the tetramer. This state of the struts could be maintained by the central complex coordinated by ankyrin-1 [23] imposing curvature on them.

Given that the fully extended struts of the cytoskeleton are  $\sim$ 200 nm long [23], basic geometry (triangle side  $a$  gives area =  $a^2 \sqrt{3}/4$ ) yields an estimate of the area of the resulting tessellation as follows: a single equilateral triangle of 200 nm on each side has an area of  $0.0173 \mu\text{m}^2$ . With a closed single-sheet surface like the RBC, each edge in the tessellation is shared with two triangles, and since there are three edges per triangle the number of triangles is  $2/3$  the number of edges. This implies that there are 80,667 triangles, which when multiplied by  $0.0173 \mu\text{m}^2$ , gives a total area of  $1397 \mu\text{m}^2$ , a number 10.9 times greater than for the real/actual RBC.

On the other hand, if we assume there are 80,667 cytoskeletal triangles, this implies a triangle area of  $128/80,667 = 0.0016 \mu\text{m}^2$ , which translates (using the triangle area formula above) to a side length of 60.8 nm. In other words, the internodal distance of the RBC cytoskeletal network should be  $\sim$ 60 nm. This number compares favourably with what we obtained as the mean distance of the edges in the tessellation analysed in Figure 2: *viz.*, 75% of the edges span 60 - 70 nm.

While the observation of a less-than-fully-extended triangular spectrin mesh could have been deduced without the complex triangularization process used here, the analysis nevertheless adds credibility to the *ab initio* triangularization process; while the discussion above confirms the consistency of the numerical values reported in the literature with a (fairly) regular triangular tessellation [23].

**Curvature.** In its present form the analysis of curvature and its graphical representation conveys a semi-quantitative impression of how the distorted RBCs might transmit the locally altered shape of the membrane to Piezo1. However, the range-of-influence of membrane curvature on Piezo1 remains to be determined. Perhaps a finer mesh of triangularization is needed to explore this. The approaches adopted here should be extendable to such situations. At the level of formal 3D differential geometry it was important to check for conformity of the total curvature with the Gauss-Bonnet Theorem [16], which states that the integral of the Gaussian curvature over a closed surface will be  $4\pi$  for surfaces like the RBC, even with its

dimples that have regions of negative curvature. Notebook 5 shows an example of this outcome in which the Gaussian curvature in each triangle was multiplied by the area of the respective triangle and then the sum taken over them all. This is tantamount to a finite difference approximation to the surface integral and was a gratifying verification of the overall curvature analysis.

## Conclusions

There are many aspects of RBC shape, volume and flexibility that are ripe for (crying out for (!) according to [34, 35], and we agree) explanation and inevitably these studies will tap into recent findings on Piezo1, and new analytical methods including computational modelling [35].

At a deeper conceptual level the work described here is an exploration of the geometrical constraints on 'biological form' (*e.g.*,[27, 36]); in this case the particular shapes are those taken up by an RBC in a strain field. The linear strain field used here is the simplest of all, being in a single direction: but it is consistent with that imposed by a stretched gel as used in our NMR experiments [14]. Much more complicated deformations occur in flowing systems, in which some domains of the RBC membrane are stressed into more positive curvature while others simultaneously undergo more negative curvature [37-40]. The ability of the RBC to accommodate these contortions decreases with the age of the cell and is posited as a major factor in what determines its survival, for ~120 days in the circulation [32]. Transient, distorted shapes exist in RBCs when they are in regions of high velocity that impose non-laminar flow around prosthetic and even healthy heart valves. Flow changes occur during valve development in cardiogenesis, in particular, and this flow is modified around calcified or diseased valves not just prosthetic ones [39, 40], so there is considerable merit in having a computationally accessible means of modelling RBC shape changes with the methods presented here.

The RBC shapes in various *in vivo* situations have begun to yield to computation. For example it is known that the stresses can be so extreme around prostheses as to lead to cell rupture. To date, such outcomes really only yield to advanced supercomputing *e.g.*, [41].

The other critical aspect of simulations for surface deformation is the distance scale of the deformations that are required to activate mechanosensitive ion channels like Piezo1 [10, 13]. The changes in curvature invoked at the tip of a patch-clamp pipette are quite extreme across a diameter of ~1  $\mu\text{m}$  or an area of 0.79  $\mu\text{m}^2$  implying that 80,667(number of triangles)  $\times$  0.79\* $(\mu\text{m}^2)\mu\text{m}^2$ , total area of RBC)  $\cong$  500 cytoskeletal triangles are spanned.

The resolution of the present simulations and the curvature near the rim of the RBC are in the same range. Therefore, if increased membrane bending activates Piezo1 then it will be those molecules at the rim of the cells (as in Figure 6, right) that would be activated. On the other hand, if a decrease in curvature (increased area of flatness) is what activates them, then it will be also found in the stretched cells. More interestingly is the fact that the two Principal Curvatures  $k_1$  and  $k_2$  *both* increase on stretching the cell (Figure 6 right).

However (as alluded to in the Introduction), in patch clamp experiments the visible curvature appears *not* to be what activates the channel. The inflation of the membrane dome is driven by the confinement by the micro-pipette that is on the micron scale. It is the tension (and presumably flattening at the nm scale below the resolution of a confocal microscope) that drives the channels to open [42-45]. Whereas in stretched/compressed gel experiments, the morphological forms taken up by the RBCs will be like those shown here. However, further curvature of the membrane on the length scale seen in membrane flickering [46, 47] would be superimposed on these shapes.

Future directions for this work will involve larger scale simulations of population-averaged curvatures in cells under strain, and in strain fields that are not simply unidirectional and linear. Then, correlations could be made with experimental measurements like those already reported on stretched/compressed gels [1, 2], and in electrophysiological measurements on whole RBCs.

## Acknowledgements

The work was funded by an Australian Research Council Discovery Project Grant DP1901005100 awarded to P.W.K., D.S., C.D.C., and P.G. Drs Soumya Mohapatra and Duncan Pettengill, consultants at Wolfram Technology Group., are thanked for advice on 3D-surface triangularization and metrification using *Mathematica*. Professor Arthur Conigrave, University of Sydney, is thanked for valuable discussions on the RBC cytoskeleton. Drs Amin Rahmat and Associate Professor Alessio Alexiadis, Engineering, University of Birmingham, UK, are thanked for collaborative work on numerically simulated (computationally intensive) shape changes in RBCs in shear fields.

## Author contributions

All authors (P.W.K., C.D.C., D.D., D.S., and P.G.) provided input into the plan of this Sub-Project (RBC shape simulation) of the ARC Discovery Project, DP190100510. This was jointly

awarded to P.W.K., C.D.C., D.S., and P.G. D.D. engaged in valuable discussions on 3D differential geometry including especially Dr Ron Goldman's valuable article [17]. P.W.K. carried out the mathematical and computational analyses and drafted the manuscript, while all authors (P.W.K., C.D.C., D.D., D.S., and P.G.) contributed to the final version.

## Competing interests

The authors declare no competing interests.

## Additional information

**Supplementary information** is available for this paper at <https://doi.org...>

**Correspondence** and requests for materials should be addressed to P.W.K.

**Reprints and permissions information** is available at [www.nature.com/reprints](http://www.nature.com/reprints).

**Publisher's note** Springer Nature remains neutral with regard to jurisdictional claims in published maps and institutional affiliations.

## References

1. Kuchel, P.W., et al., *Enhanced Ca<sup>2+</sup> influx in mechanically distorted erythrocytes measured with <sup>19</sup>F nuclear magnetic resonance spectroscopy*. Scientific Reports, 2021. **11**(1).
2. Kuchel, P.W. and D. Shishmarev, *Accelerating metabolism and transmembrane cation flux by distorting red blood cells*. Science Advances, 2017. **3** (10): p. eaao1016.
3. Coste, B., et al., *Piezo1 and Piezo2 are essential components of distinct mechanically-activated cation channels*. Science, 2010. **330**(6000): p. 55-60.
4. Ranade, S.S., et al., *Piezo1, a mechanically activated ion channel, is required for vascular development in mice*. Proceedings of the National Academy of Sciences of the United States of America, 2014. **111**(28): p. 10347-10352.
5. Archer, N.M., et al., *Heredity xerocytosis revisited*. American Journal of Hematology, 2014. **89**(12): p. 1142-1146.
6. Cahalan, S.M., et al., *Piezo1 links mechanical forces to red blood cell volume*. eLife, 2015. **4**.
7. Syeda, R., et al., *Piezo1 Channels Are Inherently Mechanosensitive*. Cell Reports, 2016. **17**(7): p. 1739-1746.
8. Gottlieb, P.A., C. Bae, and F. Sachs, *Gating the mechanical channel Piezo1: A comparison between whole-cell and patch recording*. Channels, 2012. **6**(4): p. 282-289.
9. Pei, F., et al., *The functions of mechanosensitive ion channels in tooth and bone tissues*. Cellular Signalling, 2021. **78**.
10. Guo, Y.R. and R. MacKinnon, *Structure-based membrane dome mechanism for Piezo mechanosensitivity*. eLife, 2017. **6**: p. e33660.
11. Wang, Y. and B. Xiao, *The mechanosensitive Piezo1 channel: structural features and molecular bases underlying its ion permeation and mechanotransduction*. The Journal of Physiology, 2017. **596**.6: p. 969-978.
12. Saotome, K., et al., *Structure of the mechanically activated ion channel Piezol*. Nature, 2018. **554**(7693): p. 481-486.

13. Lin, Y.C., et al., *Force-induced conformational changes in PIEZO1*. Nature, 2019. **573**(7773): p. 230-234.
14. Shishmarev, D., K.I. Momot, and P.W. Kuchel, *Anisotropic diffusion in stretched hydrogels containing erythrocytes: Evidence of cell-shape distortion recorded by PGSE NMR spectroscopy*. Magnetic Resonance in Chemistry, 2017. **55**(5): p. 438-446.
15. Kuchel, P.W. and E.D. Fackerell, *Parametric-equation representation of biconcave erythrocytes*. Bulletin of Mathematical Biology, 1999. **61**(2): p. 209-220.
16. Abbena, A., S. Salamon, and A. Gray, *Modern Differential Geometry of Curves and Surfaces with Mathematica*. 2006: Chapman and Hall/CRC. 1016.
17. Goldman, R., *Curvature formulas for implicit curves and surfaces*. Computer Aided Geometric Design, 2005. **22**: p. 632-658.
18. Mathematica, Wolfram Research, Inc. ([www.wolfram.com](http://www.wolfram.com)), *Mathematica Online*, Champaign, IL (2020).
19. Wolfram, S., *The Mathematica Book, 5th Edition*. 2003, Champaign, IL: Wolfram Media Inc.
20. Svetina, S. and B. Zeks, *Membrane bending energy and shape determination of phospholipid vesicles and red blood cells*. European Biophysics Journal, 1989. **17**: p. 101-111.
21. Grimes, A.J., *Human Red Cell Metabolism*. 1980, Oxford, UK: Blackwell Scientific.
22. Svetina, S., *Relations among variations in human red-cell volume, density, membrane area, hemoglobin content and cation content*. Journal of Theoretical Biology, 1982. **95**(1): p. 123-134.
23. Lux, S.E., *Anatomy of the red cell membrane skeleton: unanswered questions*. Blood, 2016. **127**(2): p. 187-199.
24. Sakurai, J.J. and J. Napolitano, *Modern Quantum Mechanics*. 2nd ed. 2011, Boston: Addison-Wesley.
25. Lipschutz, S., *Schaum's Outline of Theory and Problems of Linear Algebra*. 1968, New York: McGraw-Hill Book Company. 334.
26. Spiegel, M.R., *Schaum's Outline of Theory and Problems of Vector Analysis*. 1959, New York: McGraw-Hill Publishing Co. 225.
27. Coxeter, H.S.M., *Introduction to Geometry*. 1969, New York: John Wiley & Sons, Inc. 469.
28. Pan, L., et al., *Super-resolution microscopy reveals the native ultrastructure of the erythrocyte cytoskeleton*. Cell Reports, 2018. **22**: p. 1151-1158.
29. Rogers, S. and V.L. Lew, *Up-down biphasic volume response of human red blood cells to PIEZO1 activation during capillary transits*. Plos Computational Biology, 2021. **17**: p. 1-18.
30. Rogers, S. and V.L. Lew, *PIEZO1 and the mechanism of the long circulatory longevity of human red blood cells*. PLOS Computational Biology, 2021. **17**: p. 1-22.
31. Ponder, E., *Hemolysis and Related Phenomena*. 1948, London: J. & A. Churchill Ltd.
32. Lew, V.L. and T. Tiffert, *On the mechanism of human red blood cell longevity: Roles of calcium, the sodium pump, PIEZO1, and Gárdos channels*. Frontiers in Physiology, 2017. **8**.
33. Bae, C., et al., *Xerocytosis is caused by mutations that alter the kinetics of the mechanosensitive channel PIEZO1*. Proceedings of the National Academy of Sciences of the United States of America, 2013. **110**(12): p. E1162-E1168.
34. Hoffman, J.F., *Reflections of the cracked timber of red blood cell physiology*. Blood Cells, Molecules and Diseases, 2019. **79**: p. 102354 (1-8).
35. Hoffman, J.F., *Red blood cells, compasses and snap shots*. Blood Cells, Molecules and Diseases, 2018. **71**: p. 67-70.
36. Thompson, D.W., *On Growth and Form*. 1917, Cambridge, UK: Cambridge University Press. 793.
37. Sui, Y., et al., *Dynamic motion of red blood cells in simple shear flow*. Physics of Fluids, 2008. **20**(11).

38. Chung, B., et al., *Computational fluid dynamics of aggregating red blood cells in postcapillary venules*. Computer Methods in Biomechanics and Biomedical Engineering, 2009. **12**(4): p. 385-397.
39. Yu, H., et al., *A review of hemolysis prediction models for computational fluid dynamics*. Artificial Organs, 2017. **41**(7): p. 603-621.
40. James, M.E., D.V. Papavassiliou, and E.A. O'Rear, *Use of computational fluid dynamics to analyze blood flow, hemolysis and sublethal damage to red blood cells in a bileaflet artificial heart valve*. Fluids, 2019. **4**(1).
41. Alexiadis, A., *A new framework for modelling the dynamics and the breakage of capsules, vesicles and cells in fluid flow*, in *IUTAM Symposium on Dynamics of Capsules, Vesicles and Cells in Flow*, D. BarthesBiesel, M.G. Blyth, and A.V. Salsac, Editors. 2015. p. 80-88.
42. Bavi, O., et al., *Influence of global and local membrane curvature on mechanosensitive ion channels: a finite element approach*. Membranes, 2016. **6**(1).
43. Cox, C.D., et al., *Removal of the mechanoprotective influence of the cytoskeleton reveals PIEZO1 is gated by bilayer tension*. Nature Communications, 2016. **7**.
44. Cox, C.D., N. Bavi, and B. Martinac, *Origin of the force: The force-from-lipids principle applied to piezo channels*, in *Piezo Channels*, P.A. Gottlieb, Editor. 2017. p. 59-96.
45. Cox, C.D. and B. Martinac, *Bending Piezo1: The effect of amphipaths on the gating of a mechanosensitive channel*. Biophysical Journal, 2016. **110**(3): p. 349A-349A.
46. Puckeridge, M., et al., *Membrane flickering of the human erythrocyte: physical and chemical effectors*. European Biophysics Journal with Biophysics Letters, 2014. **43**(4-5): p. 169-177.
47. Puckeridge, M. and P.W. Kuchel, *Membrane flickering of the human erythrocyte: constrained random walk used with Bayesian analysis*. European Biophysics Journal with Biophysics Letters, 2014. **43**(4-5): p. 157-167.

## Figures

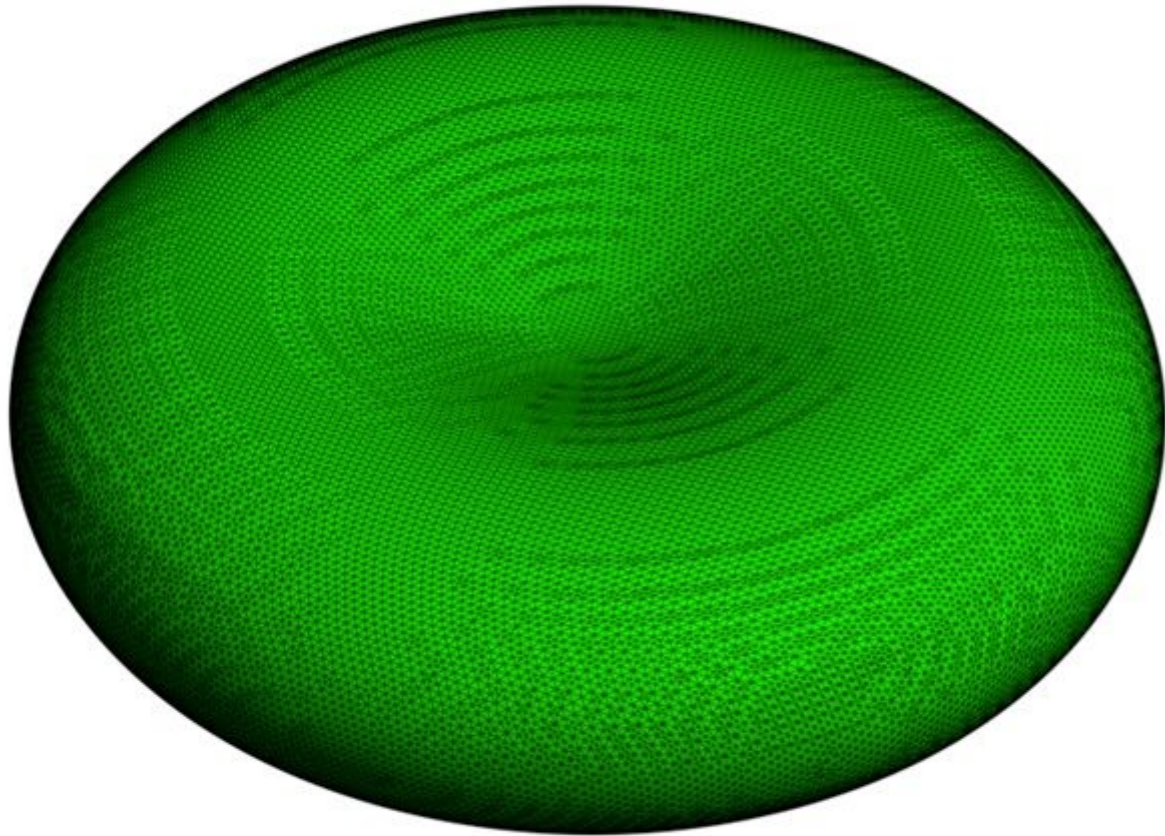


**Figure 1**

Triangular mesh of the RBC drawn to scale in its biconcave-disc, using Eq. 1 in Mathematica. The triangularization was with `BoundaryDiscretizationRegion`, applied to `ImplicitRegion` (Supplementary Information). Number of edges = 120,042 and `MeshCoordinates` gave 40,136 points and 80,268 triangles. Green colouring was chosen over red (the natural choice for an RBC) for ease of visualizing the mesh. Notebook 2 has the Mathematica script used to generate this graphic.

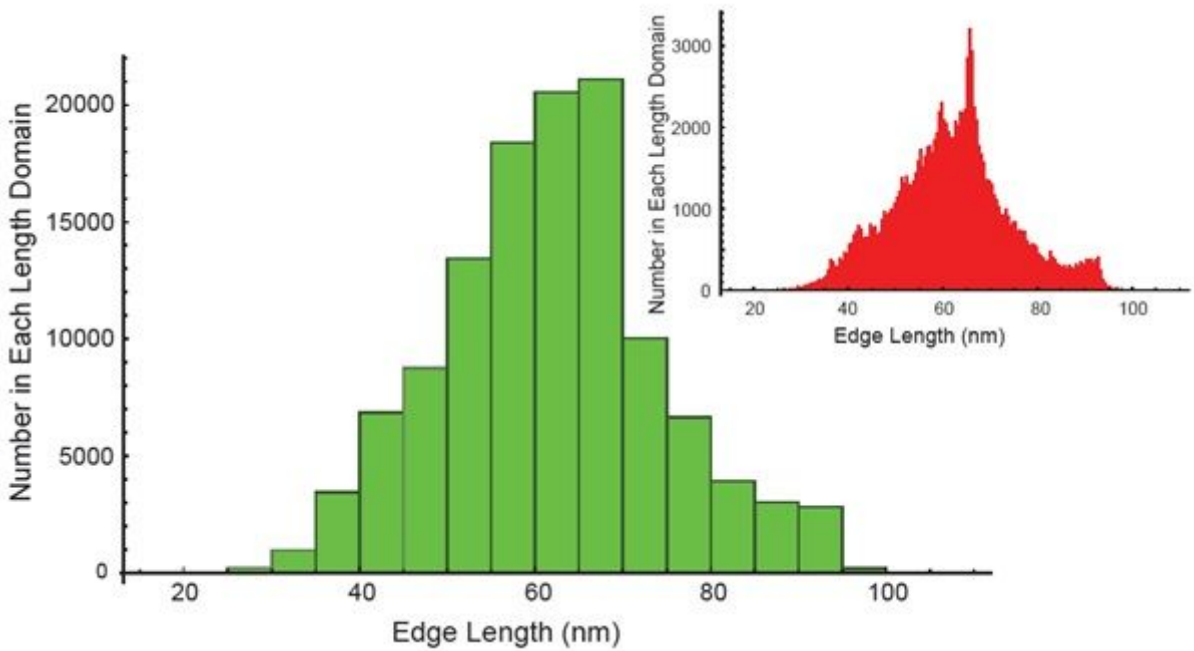


**Figure 2**

Data from the mesh in Fig.1 showing the length-distribution histogram of edges in 20 bins (green); and, 200 bins (red inset). The mean edge length overall was 62 nm. The median bin (tallest green pillar) contained 38% of the total bin contents and spanned 60 - 65 nm; while the two most abundant bins spanning 60 - 70 nm contained 75% of the edge lengths. Notebook 2 has the Mathematica script used to generate this graphic.

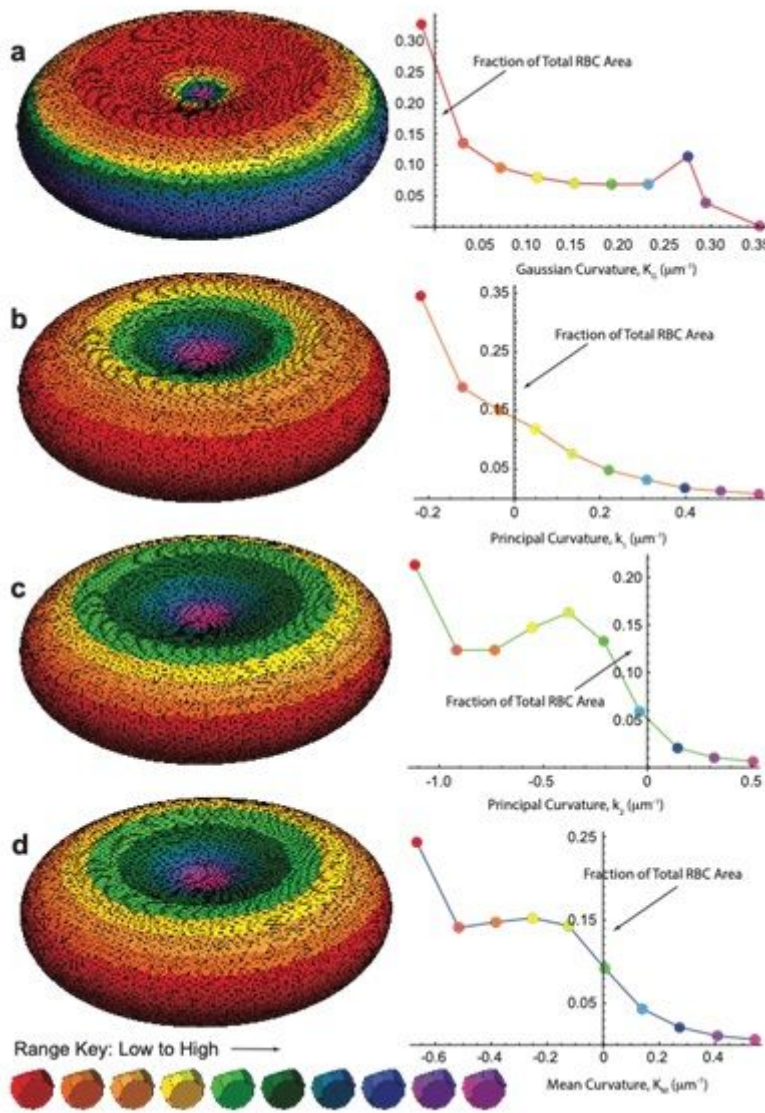


**Figure 3**

Positional dependence of the four types of curvature on the surface of the model-RBC. (a) Gaussian Curvature; (b) Principal Curvature (maximum),  $k_1$ ; (c) Principal Curvature (minimum),  $k_2$ ; and (d) Mean Curvature. On the right of each cell is the graph of mean value (of the respective curvature) versus the fraction of the RBC area that has the curvature in a specified sub-domain of values. Specifically, the minimum and maximum values of each curvature were identified, then the whole domain of values was divided linearly into 10 sub-domains (bins) with each assigned a colour-code as shown in the given Range Key. The area of each triangle was computed (Theory of Methods; and Notebook 2) so the total area occupied by triangles in a given bin was able to be expressed as a fraction of the total RBC area, 128 mm<sup>2</sup>. For speed of computation the triangulation was made with fewer mesh points than for Figure 1, specifically 13640 triangles and 6822 mesh points.

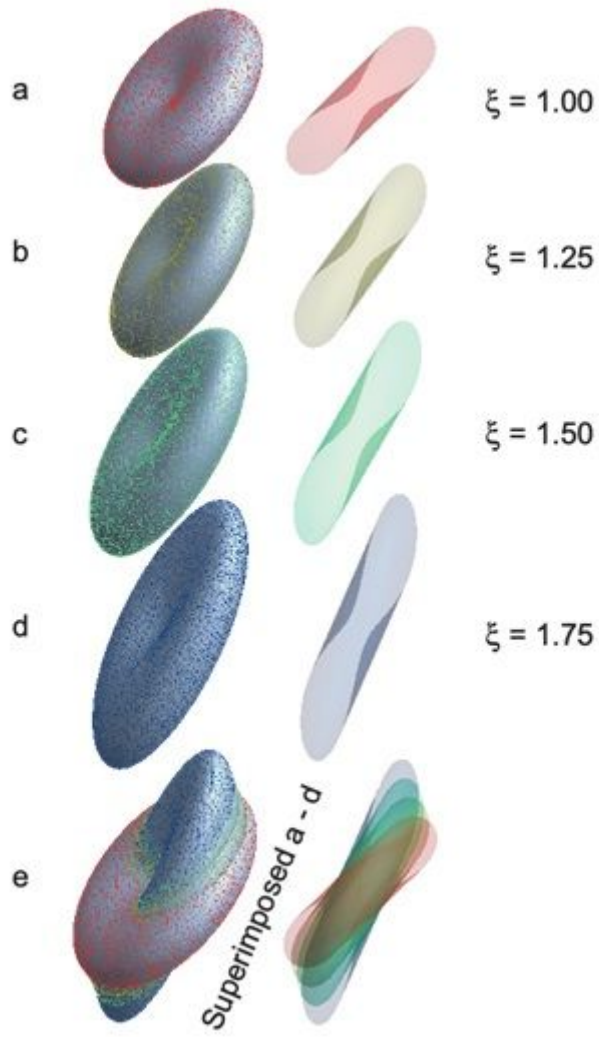


**Figure 4**

RBC rotated through  $45^\circ$  about the x-axis, relative to a linear strain field imposed in the z-direction. (a) No elongation,  $x = 1$ ; (b) stretched by 25%,  $x = 1.25$ ; (c) stretched by 50%,  $x = 1.50$ ; (d) stretched by 75%,  $x = 1.75$ ; and (e) showing the relative elongation and concomitant narrowing of the RBCs by superimposing the images. Colour coding was used to provide distinction between the RBCs in e. In the boundary discretization MaxCellMeasure was set to 0.1 giving  $\sim 8,000$  mesh points.

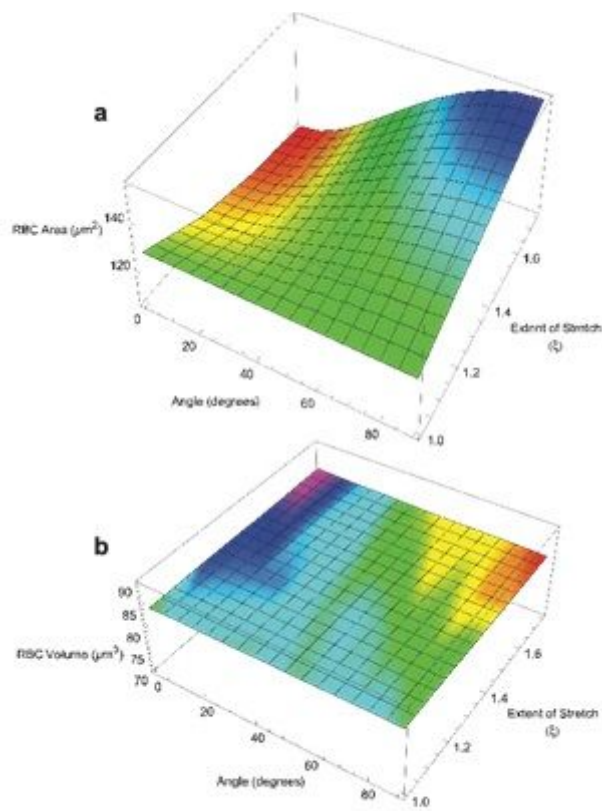


**Figure 5**

Dependence of RBC surface area (a) and volume (b) on rotation about to the x-axis ( $\alpha$ ) and stretching along the z-axis ( $\xi$ ).

### Extent of Stretching in z-Direction ( $\xi$ )

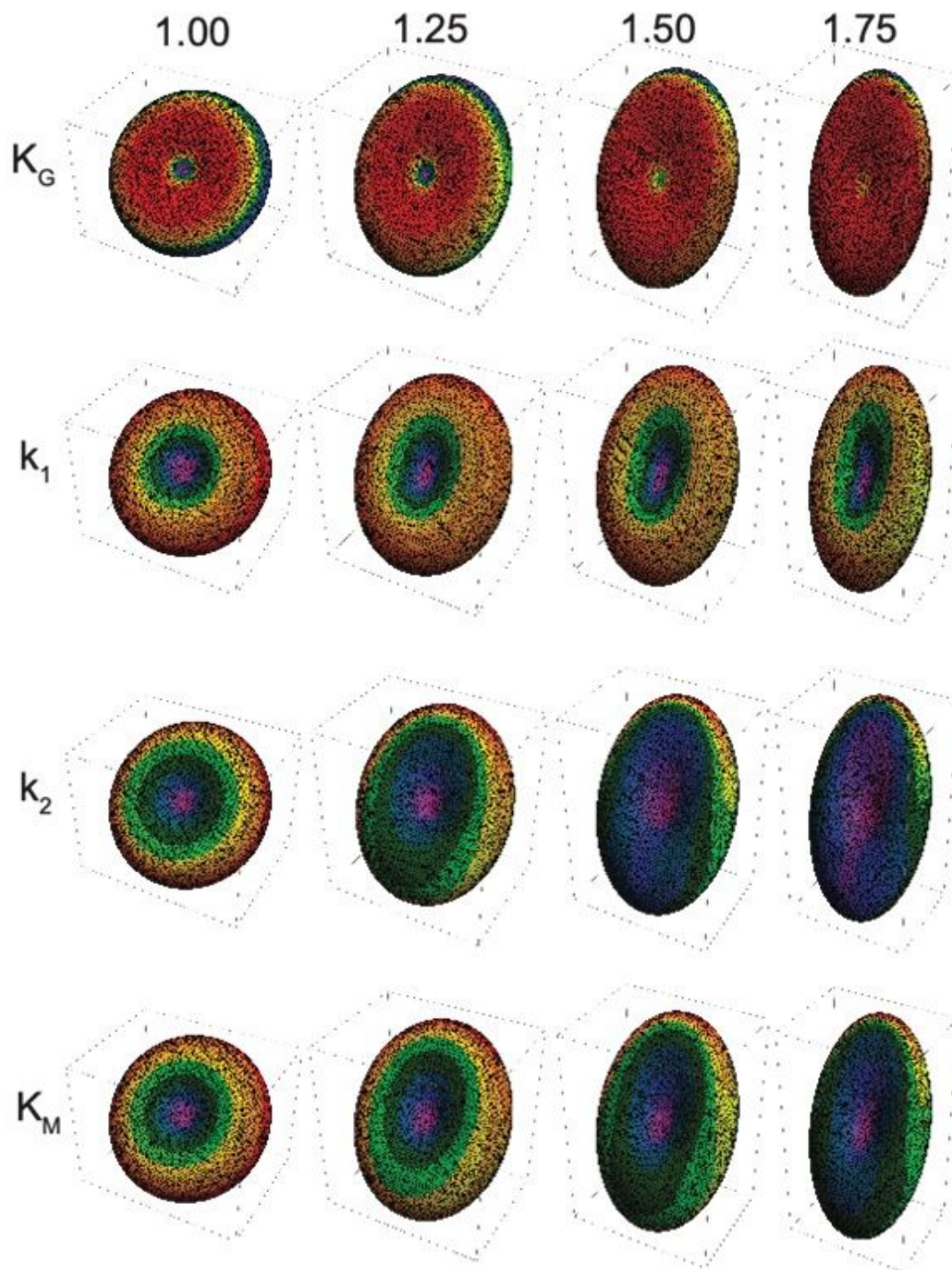


**Figure 6**

Curvatures of RBC rotated 45° around the x-axis and stretched in the z-direction by the extents ( $x$ ) indicated above.

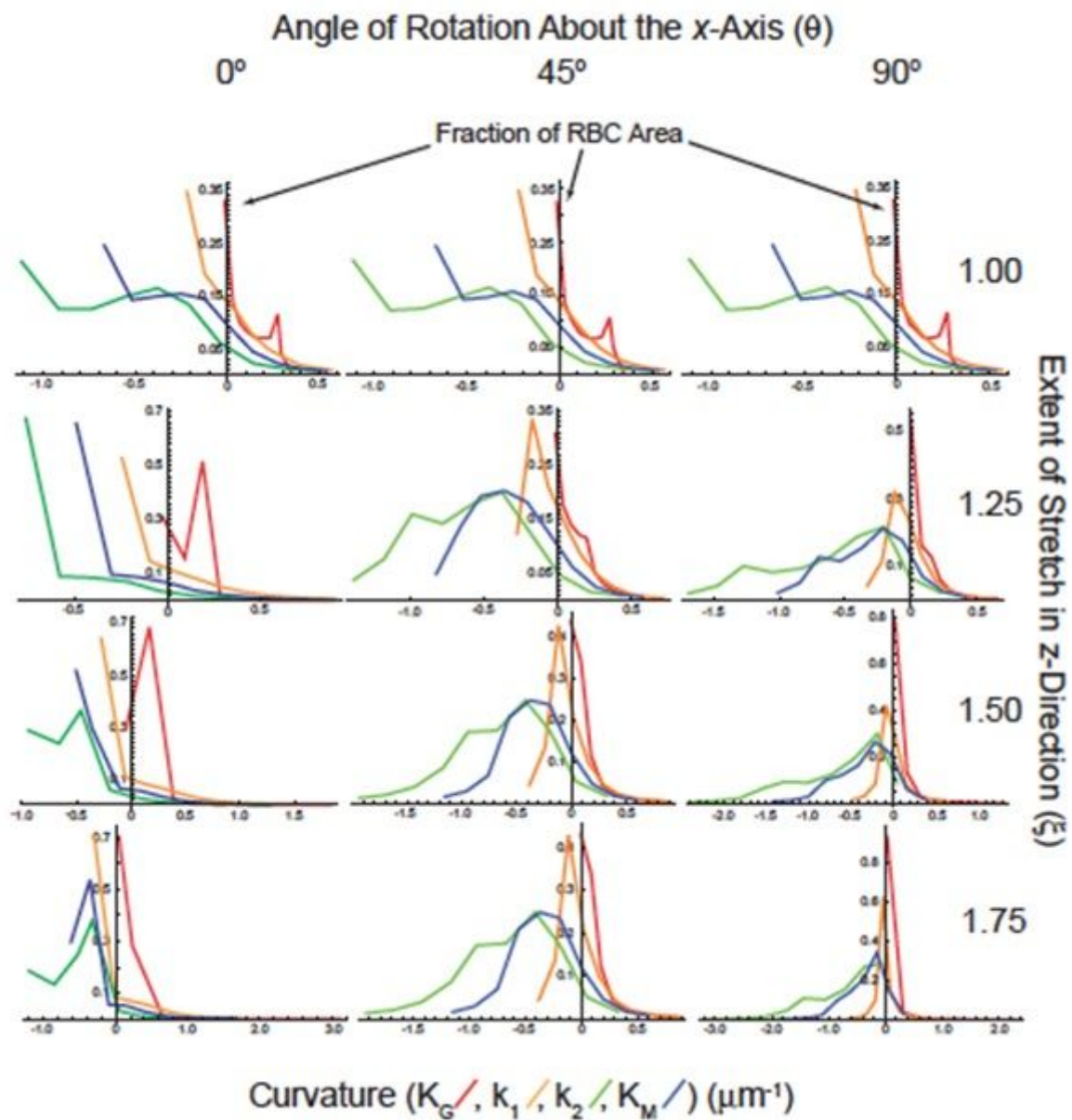


**Figure 7**

Curvature graphs of an RBC rotated at  $0^\circ$ ,  $45^\circ$  and  $90^\circ$  around the x-axis and stretched in the z-direction by the extents ( $x$ ) indicated on the right. The colours of the polygonal plots indicate: Gaussian Curvature KG, red; Principal Curvature (maximum),  $k_1$ , orange; Principal Curvature (minimum),  $k_2$ , green; and Mean Curvature KM, blue. Each discontinuity of the polygons denotes the mean value in curvature of the bin in the given curvature domain.

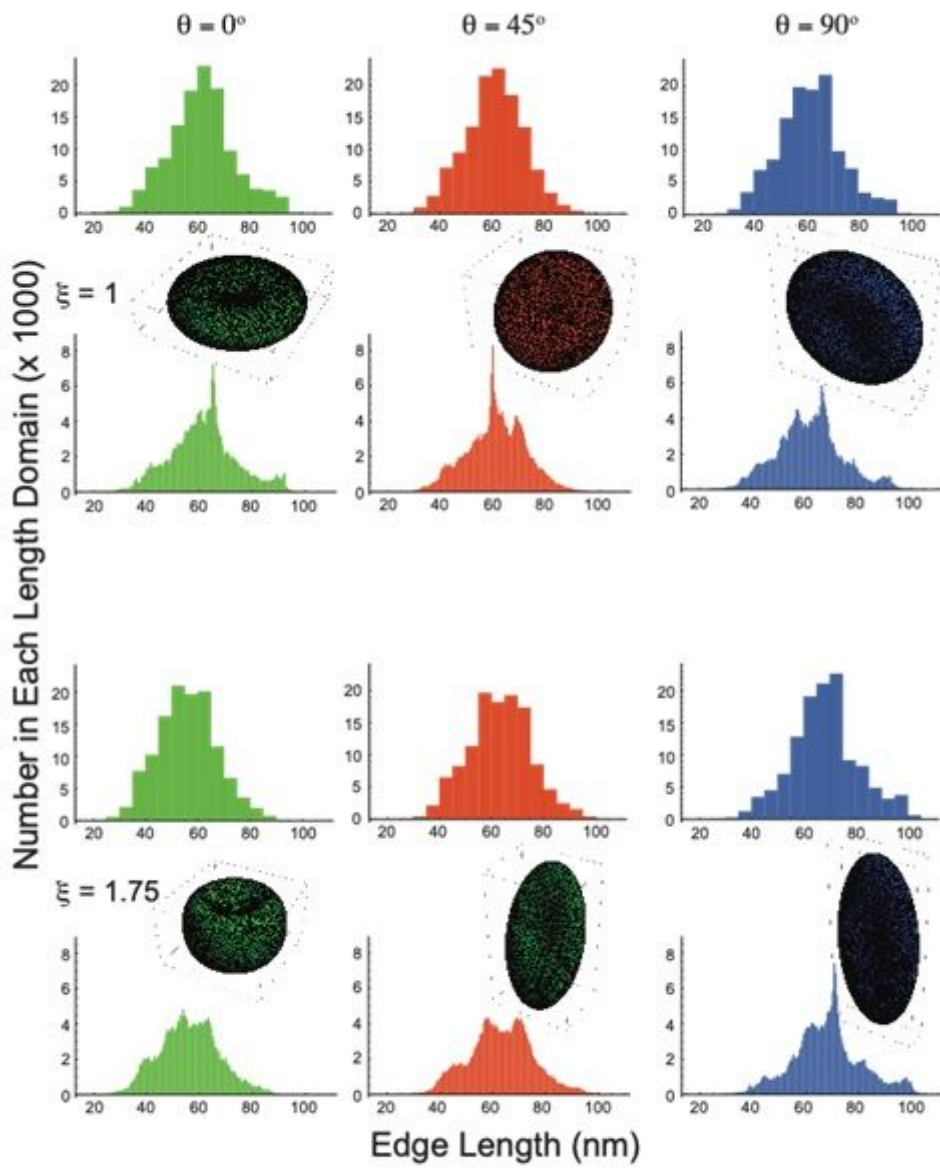


**Figure 8**

Histograms of the lengths of the 121,000 edges in the triangulation of an RBC at each of three rotations about the x-axis with no stretching ( $x = 1$ ), and 75% stretching ( $x = 1.75$ ). The colour coding was used to distinguish the three groups of data according to the rotations: green  $0^\circ$ , red  $45^\circ$ , and blue  $90^\circ$ . The bin numbers were 20 and 200 for the upper and lower pair of histograms at each value of stretching,  $x$ , respectively. The insets show the RBC shapes from which the histograms were made; they are the same as given in Figures 4, S4 and S5.

## Supplementary Files

This is a list of supplementary files associated with this preprint. Click to download.

- [RBCCurvatureSupplementaryInformation.pdf](#)